ACS OMEGA

Open Access

http://pubs.acs.org/journal/acsodf

Article

A 3-Dimensional Scaffolding System Recapitulates the Hierarchical Osteon Structure

Xiheng Li, Yalu Sun, Shuangshuang Wang, Chao Si, Huen Li, and Bei Chang*

Cite This: *ACS Omega* 2024, 9, 41368−41377

Read Online

ACCESS | Metrics & More | Article Recommendations

ABSTRACT: The bone is composed of solid cortical bone and honeycomb-like trabecular bone. Although the cortical bone provides the substantial mechanical strength of the bone, few studies have focused on its regeneration. As the structural and functional units of the cortical bone, osteons play critical roles in bone turnover. Composed of osteocytes, lamellae, lacunocanalicular network, and Haversian canals, osteons exhibit a delicate and hierarchical architecture. Studies have attempted to reconstruct the osteonal structure with artificial approaches; however, hardly the four elements were recapitulated simultaneously. In this work, a series of bioengineering techniques, including electrospinning, micropatterning, and laser-directed microfabrication, were employed to develop a three-dimensional scaffolding system, which successfully recapitulated the osteon structure *in vitro*. The physiological morphology and bioactivity of osteocytes were emulated, the intercellular communications between osteocytes were identified, and the concentric lamellae and Haversian canals were simulated as well. This work constructed an *in vivo*−like platform for osteon study, providing convenience for exploring the interaction among the osteonal elements

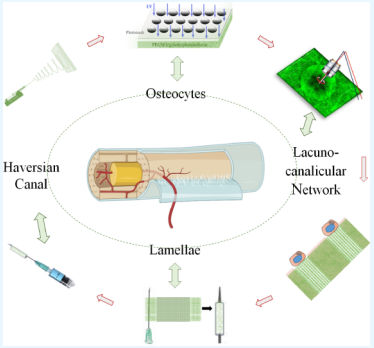

INTRODUCTION

Bone loss impacts life quality and even the survival of an individual. Representing more than 2 million worldwide each year, bone grafting has become the second most common transplant tissue.[1,2] Current bone grafting approaches possess limitations such as donor site mobility, potential of immune rejection, or pathogen transfer.[3] Therefore, using tissue engineering methods to regenerate bone has become one of the most popular research topics within the past several decades.

The bone is composed of cortical and trabecular bones. Despite that cortical bone accounts for approximately 80% of total bone mass and provides the mechanical strength and performs the major function of the bone,[4] its regeneration remains a challenge. To accommodate pluripotent stem cells with an appropriate nutrient or gas exchange, scaffolds are generally designed with a cancellous microstructure. As a result, the trabecular bone is usually formed, while cortical bone regeneration is scarcely detected. Since the transition of the trabecular bone to the cortical bone requires a prolonged remodeling process before mechanical strains can be loaded,[5] direct cortical bone regeneration will dramatically reduce the postsurgical rehabilitation time for orthopedic-surgery patients. Therefore, direct regeneration of cortical bone in orthopedic research is of imperative clinical significance.

Cortical bone regeneration relies on functional recapitulation of its basic constituent units, osteons. Cortical bone is formed by parallelly assembled osteons that present a complicated hierarchical architecture. An osteon displays a cylinder morphology with multiple concentric osteocyte-containing lamellae that surround a central Haversian canal. Together with the lacunocanalicular network (LCN) that accommodates osteocyte cell body and dendrites, osteocytes, lamellae, and Haversian canal form a delicately communicative network that supports the physiological function and turnover of the cortical bone.

With the unmask of its significance in physiological bone functions, osteons have become one of the most popular topics in the field of bone biology. Particularly, mathematical models[6] and mechanical tests[7−9] have facilitated our in-depth understanding of osteons, and the rational underlying the critical role of osteons in mechanical loading resistance have been somewhat unveiled. Generally, osteocytes and LCN sense and transduce external mechanical stress, and the concentric lamellae reduce bone porosity and function as a rigid shield to resist repetitive mechanical loading. In the meantime, the development of cytological or scaffolding approaches to recapitulate the osteonal structure *in vitro* was still immature.[10] As shown in previous studies, hydrogels, microparticles, or micropatterning techniques were generated to simulate the

Received: April 30, 2024
Revised: September 11, 2024
Accepted: September 16, 2024
Published: September 24, 2024

morphology and physiological functions of osteocytes. Three-dimensional (3D) printing or electrospinning-rolling methods were used to imitate concentric lamellae. Meanwhile, bottom-up, casting, or extrusion approaches were employed to recapitulate the Haversian canal. However, the integral configuration of osteons that include all four osteonal elements, namely, osteocytes, lamellae, the LCN system, and the Haversian canal, have not been reconstructed simultaneously due to the complexity in osteon structure and the intricate interaction among those elements. As a result, the molecular mechanism underlying the mechanosensation and mechanotransduction of osteons remain unclear. Therefore, the development of a novel scaffolding system that reconstructs the integral osteonal structure is of critical importance.

We recently developed a 3D bioinspired scaffolding system that emulated the physiological extracellular matrix (ECM) microenvironment and accommodated osteocytes *in vitro*. BMSCs cultured within the system exhibited an osteocyte-like morphology with a satellite-like cell body residing on the microisland and multiple dendrites protruding into the microchannels. To be noted, this scaffolding system deprived cell−cell communication and provided a unique platform for exploring single osteocyte behaviors extensively. We deepened our exploration with this bioinspired system by focusing on its role in modulating the morphological and functional osteoblast-to-osteocyte transitions. Moreover, considering that osteocytes are accommodated within a hierarchical osteonal system, we further expanded our system by adding a matrix rolling procedure to imitate the concentric lamellae and explored the intercellular communication between BMSCs residing within adjacent lamellae. In the meantime, a HUVEC/Matrigel injection procedure was employed to recapitulate the Haversian canal within the innermost of an osteon. In this way, we successfully emulated the integral structure of an osteon *in vitro*, which not only provided a novel and comprehensive platform for exploring the interactive communication among the osteonal elements but also set an example for the development of next-generation cortical bone regeneration approaches.

MATERIALS AND METHODS

Scaffold Fabrication. The generation of nanofibrous microisland and the canaliculi was performed as previously described.[11] Briefly, the GelMA nanofibrous matrix was first fabricated with an electrospinning technique, followed by immersion in a PEGDA/photoinitiator aqueous solution for photolithography. Then, the patterned matrix was loaded onto a PEN slide for laser drilling under a laser microdissection machine (Leica LMD7000) to generate lacunae-like microchannels. Afterward, the matrix was sterilized, washed, and then flattened on a predesigned membrane holder for BMSC seeding. The cell-laden matrix was smoothened out on a glass slide and a 30-gauge syringe needle was placed above the matrix. Rolling around the needle, the matrix formed a concentric morphology in a sterilized environment. Right after the rolling, a syringe containing HUVEC/Matrigel was connected to the needle, and with the retraction of the needle, the HUVEC/Matrigel complex was injected inside the axis cylinder of the rolled matrix.

Cell Culture. Human bone marrow stem cells (BMSCs), human umbilical vein endothelial cells (HUVECs), and endothelial cell growth media kits (EGM-2 BulletKit) were purchased from Lonza. BMSCs were cultured in an ascorbic acid−free a-modified essential medium (a-MEM) (GIBCO, Invitrogen, Carlsbad, CA) supplemented with 10% fetal bovine serum (FBS) (Invitrogen) and 1% penicillin−streptomycin (Invitrogen) in a humidified incubator with 5% CO_2 at 37 °C. The culture medium was changed every 2 days, and BMSCs of passages 3−5 were used for the experiments. One h after 2×10^4 BMSCs were seeded onto 1 cm^2 of microislands, unattached cells were washed off the matrix by gently pipetting up the culture medium. The BMSC/matrix were cultured for 3 days before rolling and HUVEC injection. HUVEC were cultured in the EGM-2 Bullet Kit following manufacturer's instruction. For HUVEC/Matrigel injection, 5×10^5 HUVECs within 50 μL of medium was mixed with 50 μL of precooled 1:3 diluted Matrigel (BD Biosciences) and loaded within the syringe. For one rolled BMSC-laden matrix, 30 μL of HUVEC/Matrigel was injected. Afterward, the BMSC/matrix/HUVEC/Matrigel system was placed within the 37 °C incubator for 20 min for gelation.

Cell Staining and Imaging. The cell-microisland construct was rinsed with DPBS and fixed with 4% PFA for 30 min. The F-actin staining was operated following the manufacturer's instruction (CF633 phalloidin, Biotium 00 046), followed by nuclei staining with Hoechst 33342 (5 mg/mL, Thermo Scientific 62 249) for 15 min and washed with PBS in triplicate.

For immunofluorescence staining, samples were blocked in 5% goat serum for 4 h at room temperature and reacted with first antibodies and CF633 phalloidin (10 U/ml, Biotium 00 046) overnight. After being washed with PBS for 3 times, the samples were stained with Alexa Fluor Plus 555 secondary antibody (1:200, Invitrogen, A32732) for 2 h, followed by 1 μg/mL Hoechst 33 342 for 20 min. The samples were washed and mounted with coverslip (CoverWell Imaging Chamber Gasket). The first antibodies used were listed as follows: Sclerostin (Abcam #85799, 1:200), DMP-1 (Invitrogen #PA5−57956, 1:150), ORP150 (Abcam #134944, 1:250), MEPE (Invitrogen #PA5−58205, 1:100), Runx2/Cbfa1- (Abcam #192256, 1:500), Casein Kinase II (R&D #AF4380, 10 μg/mL), Osterix (Abcam #209484, 1:400), osteocalcin (Abcam #93876, 1:200), and E11/gp38/podoplanin (Abcam #128994, 1:200).

For confocal observation, directly mounted samples were used for taking top-view images. Three samples, including at least 100 single cell-laden microislands, were collected for analysis. To obtain lateral view of cells, the stained samples were embedded in an OCT and processed with freezing microtome section. Sections with a thickness of 20 μm were harvested and immediately mounted with a coverslip. At least 90 lateral images from 3 samples were collected for analysis. High-resolution images were taken in stack mode with a 0.4-μm step size. Image files were also exported for 3D reconstruction using Imaris 9.0.

For SEM observation, each sample was dehydrated with a graded ethanol solution (50%, 70%, 95%, and 100%, 30 min for each), dried in a vacuum oven, coated with gold with a sputter coater (SPI-module Sputter Coater Unit, SPI Supplies/Structure Probe, Inc.), and observed under an SEM machine (JSM6010, JEOL).

Statistical Analysis. Quantitative results were presented as the mean ± standard deviation (SD). The unpaired Student's *t*-test was used to test the significance between two groups. A value of $p < 0.05$ was considered statistically significant.

https://doi.org/10.1021/acsomega.4c04146
ACS Omega 2024, 9, 41368−41377

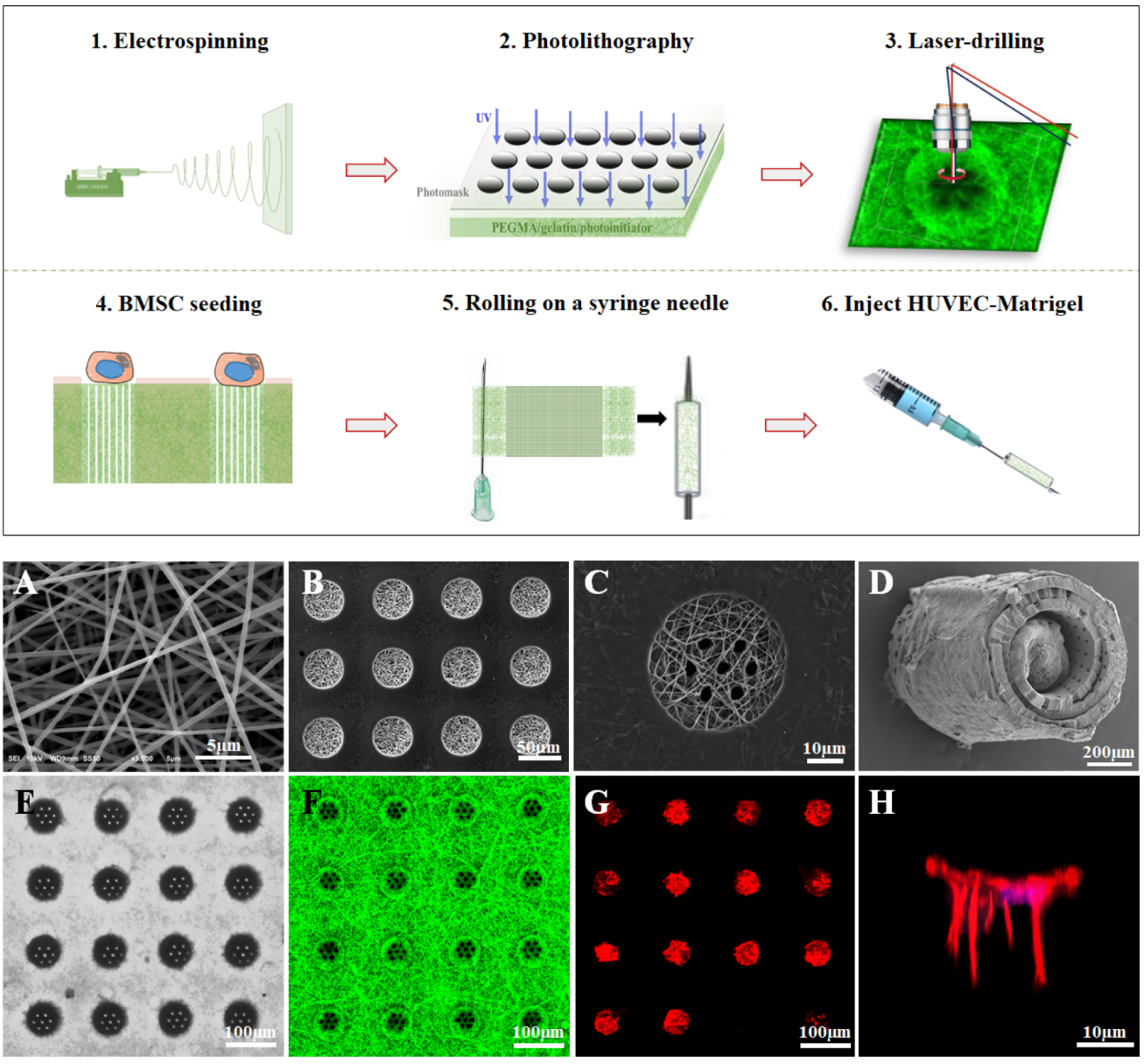

Figure 1. Top: Scheme showing the fabrication process of the Osteon-mimicking scaffolding (OMS) system. OMS was generated *via* an electrospinning process, a photolithography process, a laser-drilling process, cell seeding, a rolling process, and a HUVEC/Matrigel injection process. Created with permission from BioRender.com. Bottom: (A) showed the ECM-like nanofibrous network of the OMS matrix, which was generated *via* electrospinning. (B) showed the organized alignment of the cell-selective microislands, which were generated *via* photolithography. (C) showed an enlarged microisland with seven microchannels formed *via* laser-drilling. (D) showed the morphology of an integral OMS, which was composed of microisland-concentrical lamellae. (E) and (F) showed the morphologies of microislands before cell accommodation under light microscopy and fluorescence microscopy, respectively. (G) showed BMSC seeding on the microislands. (H) showed the typical morphology of one single osteocyte-like BMSC cell (OLC) on the OMS *via* 3D confocal image reconstruction. Red indicated actin-binding phalloidin, and blue indicated the nucleus.

RESULTS AND DISCUSSION

As shown in Figure 1, a series of techniques were employed to generate the osteon-mimicking scaffolding (OMS) system. First, a GelMA-based matrix was fabricated via electrospinning. The resultant matrix exhibited a nanofibrous topography formed by interweaving GelMA nanofibers with a diameter of 200−500 nm, similar to the nature bone ECM (Figure 1A). Then, the GelMA matrix was employed as the substrate for a photolithography process, forming isolated cell-adhesive GelMA-exposed microislands surrounded by cell-repellent PEG-coated regions (Figure 1B). With this approach, cell clusters got dispersed, and the attachment of single BMSCs on each microisland was achieved, which simulated the isolated distribution of *in vivo* osteocytes. Afterward, a laser ablation technique was used to create canaliculi-like microchannels within the microislands. According to our previous work, microisland surface area not only played a critical role in determining single cell ratio and cell spreading[11] but also greatly influenced the polarized morphology of single cells together with the microchannel diameter.[12] Thus, in this work, circular microislands with a surface area of 1800 μm^2 were selected, which mostly resembled the BMSC size in traditional cell culture methods, and seven microchannels with an average

https://doi.org/10.1021/acsomega.4c04146
ACS Omega 2024, 9, 41368−41377

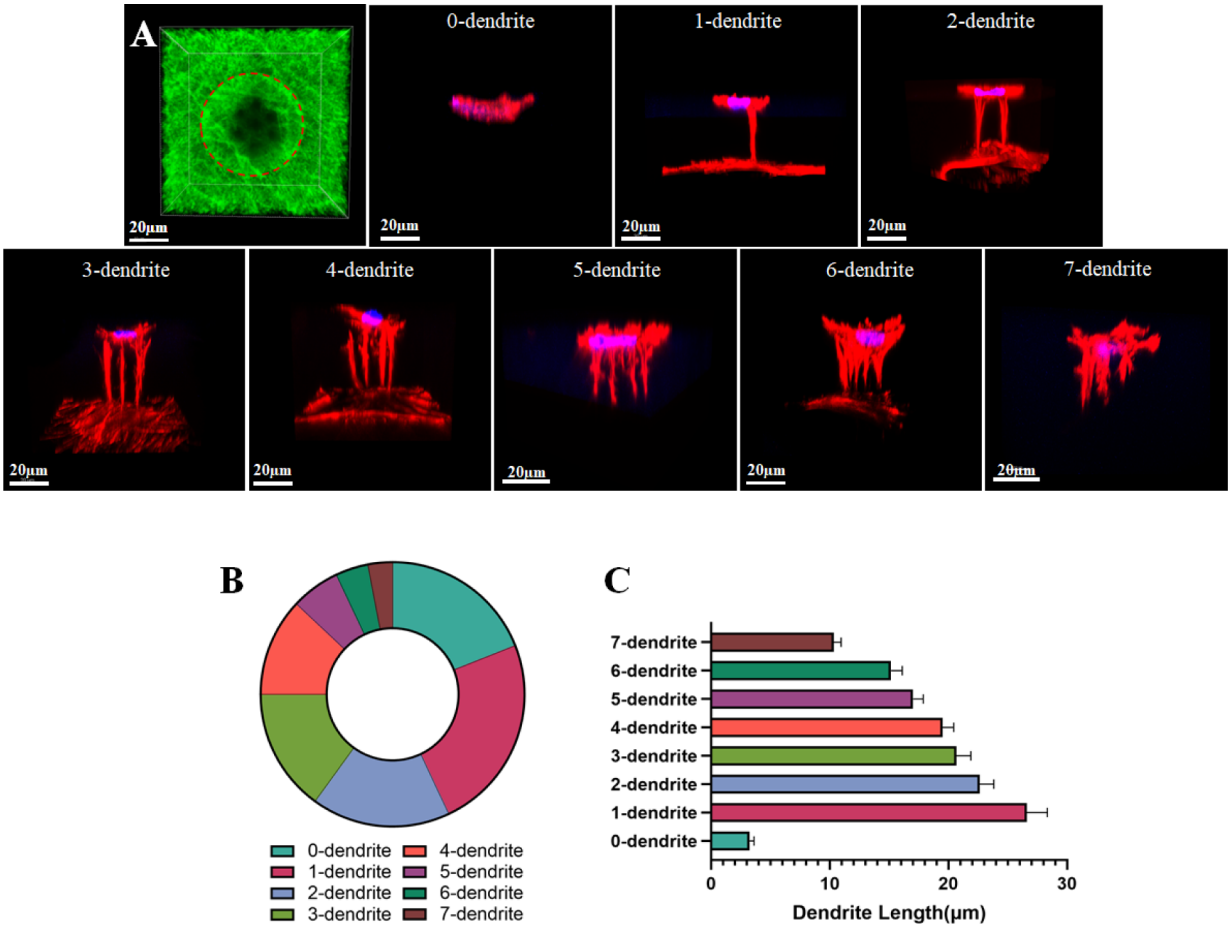

Figure 2. Morphology of single BMSCs on a laser-drilled microisland. (A) Single BMSCs formed 0−7 cellular dendrites on the microisland. Red indicated actin-binding phalloidin, and blue indicated nucleus. (B) showed the distribution of single BMSCs in the number of dendrites formed within the microislands. (C) showed the average lengths of BMSC dendrites. More than 300 single BMSCs from 3 samples were captured and recorded for dendrite meansurement. Data were presented as mean ± SD.

diameter of 2.6 μm (2.6 ± 1.1 μm) were generated within each microisland (Figure 1C,E,F) for illustration, although each osteocyte was reported to possess an average of 114.5 dendrites.[13] Following cell seeding, the patterned matrix was rolled around a needle syringe, forming a concentrical shape similar to the lamellae of nature osteons. In the meantime, a HUVEC/Matrigel complex was injected inside the central cylinder space of the rolled matrix, which emulated the Haversian canal. In this way, an osteon-mimicking system was generated, with an average diameter of 700−800 μm and an average length of 4−5 mm (Figure 1D).

After BMSCs were trypsinized and seeded on the patterned matrix, cells occupied only within the microisland area and were isolated from neighboring cells, exhibiting an exceptional surface selectivity of the system. Quantitative analysis showed that over 78.3% of the microislands got occupied by cells and among those, 47.5% accompanied by single cells, showing ideal biocompatibility of the system (Figure 1G). As the most common cell type in bone (over 90% of all bone cells), osteocytes are terminally differentiated bone cells with a stellate-shaped cell body and a number of dendritic processes originating from the cell body. Osteocytes line up orderly within osteon lamellae, and their longitudinal axes are parallel to the lamellae in which they reside. Single BMSCs cultured on the OMS displayed a typical polarized morphology that the cell body resided on the surface of microisland while multiple dendrites invaded within the laser-drilled microchannels (Figure 1H), similar to the *in vivo* osteocytes.

Together with the cell body, osteocyte dendrites comprise the functional parts of an osteocyte. It is known that osteocytes play critical roles in mechanosensantion, although the molecular mechanism remains controversial[14] that various components of an osteocyte, including its dendrites, cell body, primary cilia[15] and integrin receptors on the cell membrane,[16] have been proposed to be responsible. Among them, osteocyte dendrites mainly function through sensing bone fluid flow shear stress within LCN.[17,18] Moreover, dendrites play critical roles in osteon turnover. When microcracks invoked damage to dendrites, the osteocyte would launch apoptosis and meanwhile send signals (e.g., RANKL) to adjacent viable osteocytes to activate osteoclastogenesis and initiate local bone remodeling.[19,20]

In order to emulate the osteocyte dendrites, seven microchannels were fabricated within each microisland in this work. Stacked images of single BMSCs were generated via a confocal microscope. Only when a cellular process originating from the cell body was longer than 5 μm, it was recorded as a dendrite. Quantitative analysis showed that over 80% of single BMSCs on the OMS formed more than one dendrite; thus, those cells were named osteocyte-like cells (OLCs) (Figure 2). Among the 335 cells calculated, about 19.1% single BMSCs formed no dendrites, 23.9% formed 1

https://doi.org/10.1021/acsomega.4c04146
ACS Omega 2024, 9, 41368−41377

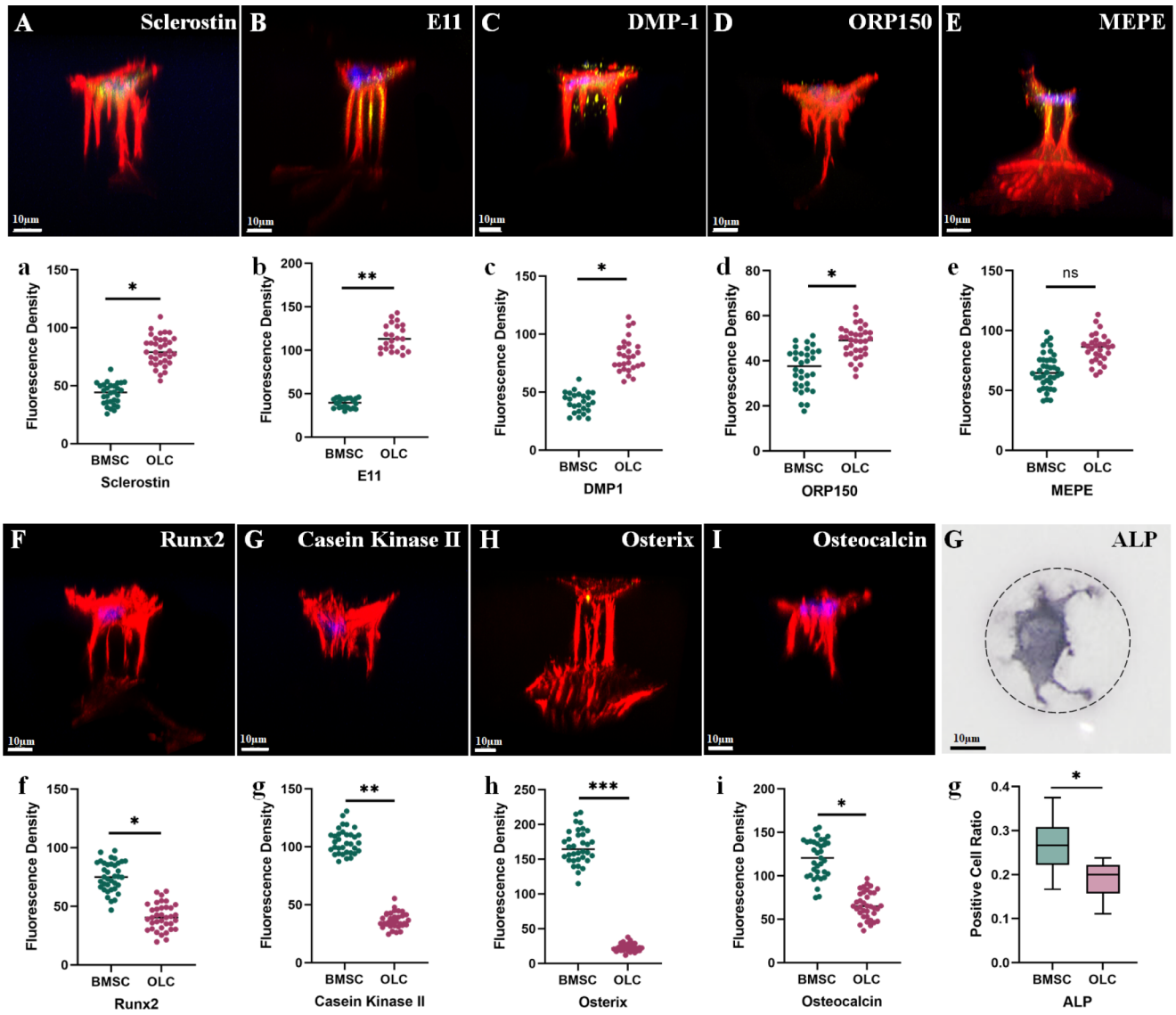

Figure 3. Expression of osteoblast-indicating and osteocyte-indicating markers on OLCs, including upregulated markers like Sclerostin (A), E11 (B), DMP-1 (C), ORP150 (D) and MEPE (E), and downregulated markers like Runx2 (F), Casein Kinase II (G), Osterix (H), Osteocalcin (I) and ALP (G). Red indicated actin-binding phalloidin, yellow indicated the specific markers and blue indicated nucleus. (a-g) showed the semiquantitative data of the expression levels of these markers. Unpolarized single BMSCs (without the formation of dendrites) cultured on the same scaffold were selected as the control group. In each group, at least 30 cells were recorded. Data was presented as mean ± SD, * indicated $p < 0.05$, * indicated $p < 0.01$ and *** indicated $p < 0.001$.

dendrite with an average dendrite length of 26.6 μm, 17% formed 2 dendrites with an average length of 22.6 μm, 14.9% formed 3 dendrites with an average length of 20.7 μm, 12.2% formed 4 dendrites with an average dendrite length of 19.5 μm, 6% formed 5 dendrites with an average dendrite length of 17.1 μm, 4.2% formed 6 dendrites with an average dendrite length of 15.2 μm, and 3.3% formed 7 dendrites with an average dendrite length of 10.3 μm. As reported by previous work, the average thickness of lamellae within osteons usually ranged from 4 to 7 μm;[21] therefore, the OLC dendrites should be able to penetrate across multiple lamellae. These results indicated that single BMSCs cultured on this novel bioinspired scaffold are morphologically similar to *in vivo* osteocytes in which dendrites not only probe through lamellae and communicate with adjacent cells within an osteon but also pervade cement line (the outermost layer of an osteon) and anchor to the surrounding interstitial bone, establishing communications between osteons and interstitial bone matrices.[22]

The transition from osteoblasts to osteocytes indicated the maturation of the osteonal bone. In *in vivo* microenvironments, osteoblasts are encased and gradually transform to osteocytes with the deposit of bone matrix. During this process, in addition to morphological changes such flattening of the cell body , formation of dendrites, and reduction in cell volume, changes in biomarker expression occur as well. Particularly, the expression of osteoblast-specific markers including Osterix, ALP, OCN, Runx2, and Casein Kinase II decreased or disappeared, while those of osteocyte-specific markers such as DMP-1, FGF23, ORP150, sclerostin, and OF45/MEPE increased.[23,24] In order to examine the functional status of single BMSCs on microislands, immunofluorescence staining of these biomarkers was performed. Polarized BMSCs (OLCs) were imaged and evaluated as the experimental group, and

https://doi.org/10.1021/acsomega.4c04146
ACS Omega 2024, 9, 41368−41377

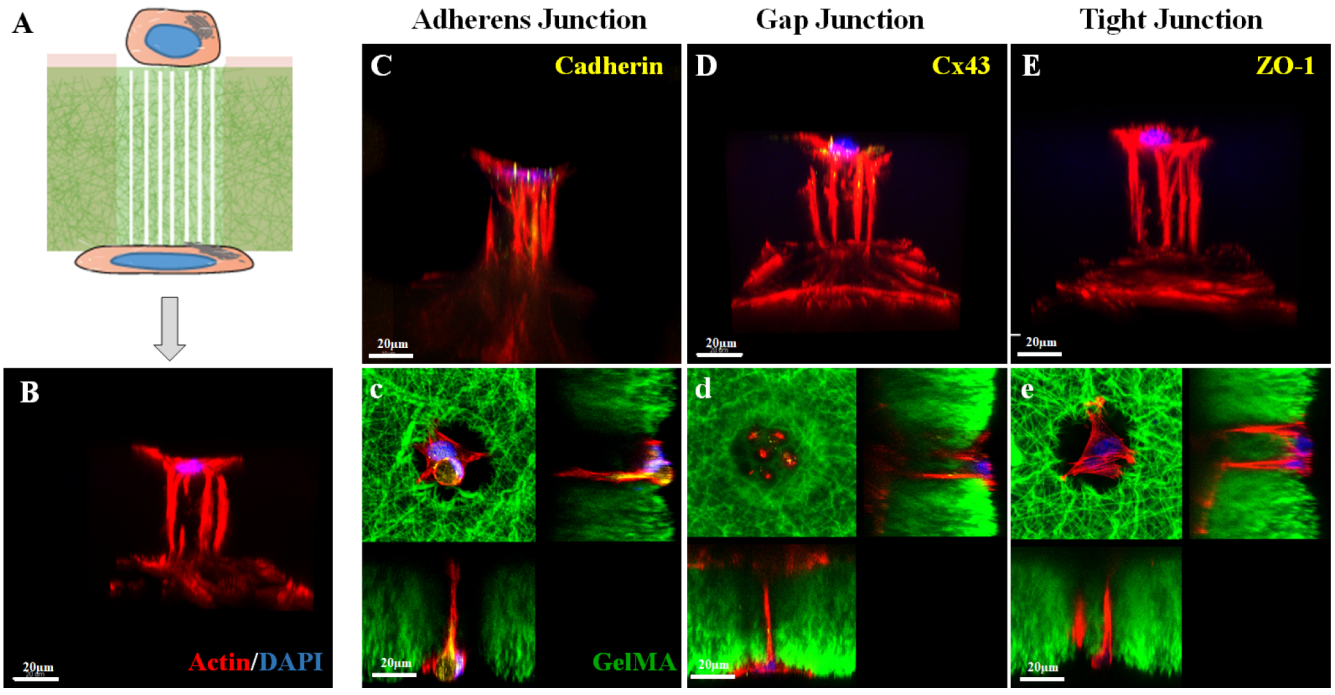

Figure 4. Intercellular communication among two OLCs between adjacent lamellae. The scheme (A) and 3D confocal reconstructed image (B) show the cell seeding and communication. (C) indicated the formation of adherens junction among adjacent OLCs. (D) indicated the formation of gap junction among adjacent OLCs. Tight junctions were not detected among the OLCs (E). Green indicated FITC-labeled GelMA-based scaffold (OMS), red indicated actin-binding phalloidin, yellow indicated the specific markers, and blue indicated the nucleus.

nonpolarized BMSCs on the same GelMA microislands with same canalicular structures were selected as the control group (Figure 3). As the quantitative data showed, OLCs expressed significantly higher levels of Sclerostin (186.64%), DMP-1 (196.87%), and ORP150 (132.89%) and a relatively higher level of MEPE (128.43%) than nonpolarized BMSCs. Meanwhile, the OLCs displayed lower levels of Runx2 (54.33%), Casein Kinase II (34.97%), Osterix (13.61%), and osteocalcin (55.39%). Here, the level of E11/gp38, a marker specifically expressed on the cell body and dendrites of embedding osteoid osteocytes, was also examined since it was reported to control the formation, elongation, and mechano-responsiveness of osteocyte dendrites. Moreover, the expression level of E11 is regulated by external stimuli such as mechanical strains.[25] As shown in Figure 3B(b), E11 was evidently expressed in the dendrites of OLCs, and its expression level was significantly accelerated (292.86%) compared to control BMSCs, further confirming that the micropatterned canalicular system facilitated the commitment of BMSCs into osteocyte lineage. In the meantime, the ALP-positive single-cell ratio decreased dramatically from 26.64% in BMSCs to 18.62% in OLCs (Figure 3G(g)). The changes of these biomarker expressions were in accordance with *in vivo* osteoblast-to-osteocyte transition, indicating that this novel OMS system induced osteocyte differentiation both morphologically and functionally.

Osteocytes communicate frequently with neighboring cells from the same or adjacent lamella, although they do not assemble densely in an aligned layer such as osteoblasts or odontoblasts. Cross-sectional images of mature osteons have shown that canaliculi where osteocyte dendrites reside form a vastly interactive network across lamellae. Considering the large number of dendrites (114.5 dendrites per osteocyte) and the vast volume of canaliculi (115.3 μm^3 per osteocyte),[13] exceeding communication among osteocytes is expected *via* LCN. In this work, by generating microchannels perforated throughout the matrix and seeding BMSCs on both sides (Figure 4A), we managed to observe the intracellular communication between OLCs resided in adjacent lamellae. Since the patterned microislands could not be generated at exactly the same spot on both sides of the matrix due to technique limitations, BMSCs seeded on the nonpatterned side spread freely (Figure 4B). Nevertheless, by selecting microislands with one nucleus on each side of the matrix and reconstructing the cell−matrix interaction, the cell−cell contact between the OLCs can be detected within the microchannels.

According to previous studies, osteocyte communication majorly occurs between dendrites from adjacent cells, either by transduction of interstitial fluid flow within LCNs or by direct dendrite−dendrite contact.[10] Previous studies have detected the presence of adherens junction and gap junction between osteocytes,[26] while the formation of tight junction remains controversial.[26,27] In order to investigate the communicative mechanism among the OLCs, immunofluorescence images of biomarkers representing these junctions were captured. As shown in Figure 4, adherens junction (Cadherin, Figure 4C(c)) and gap junction (Cx43, Figure 4D(d)) were clearly spotted between OLCs from adjacent lamella, while the formation of tight junction (ZO-1, Figure 4E(e)) can hardly be observed. Although the existence of tight junctions requires further exploration, this result is consistent with that between *in vivo* osteocytes. Moreover, it should be noted that in nature osteons, canaliculi also exist between osteocytes residing within the same lamellae; however, such phenomenon was not observed in this system due to the slow degradation of PEG. In order to solve this problem, we are working on a new approach

https://doi.org/10.1021/acsomega.4c04146
ACS Omega 2024, 9, 41368−41377

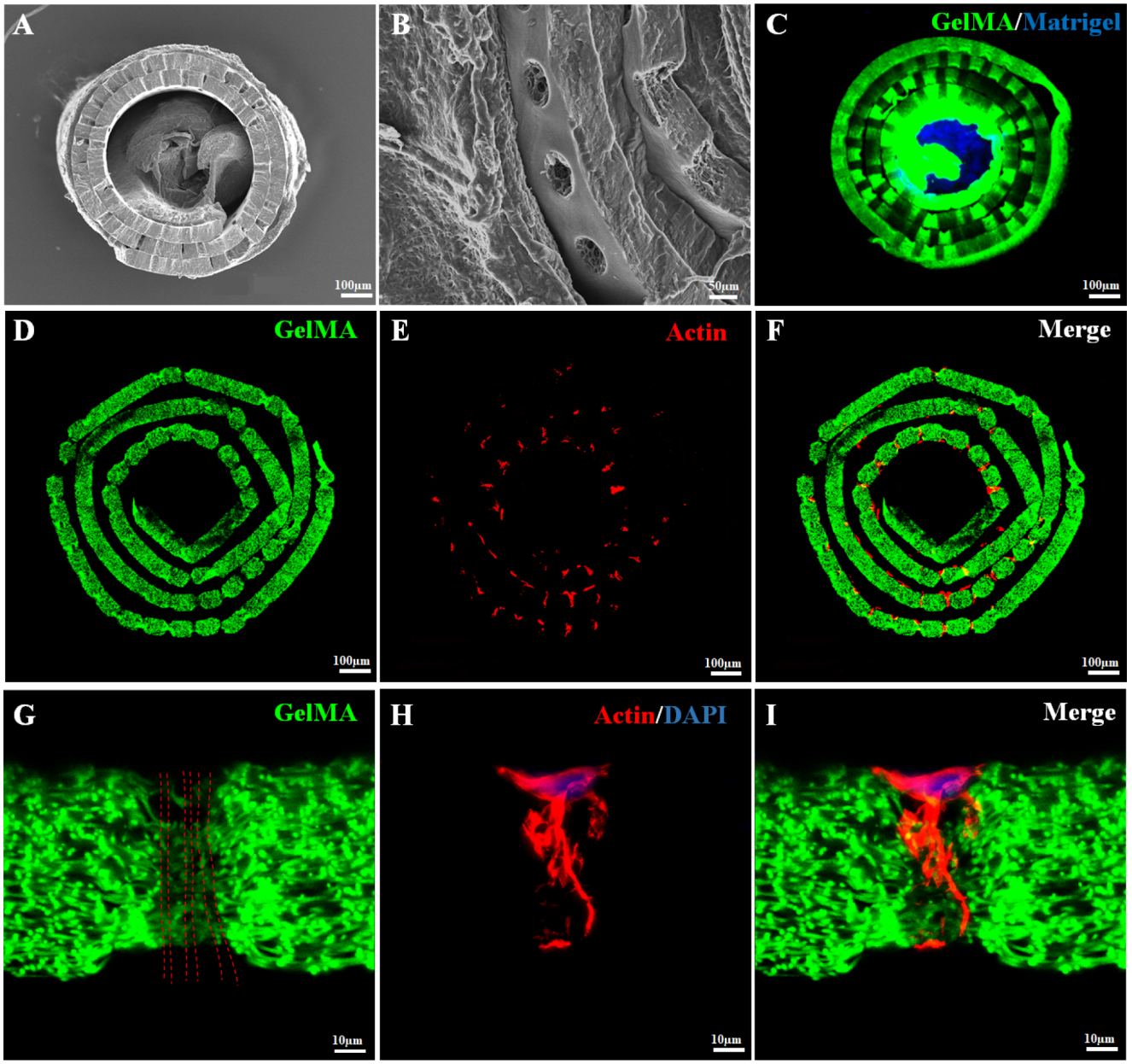

Figure 5. Recapitulation of the concentric lamellae of the OMS system. (A−C) SEM and confocal images of an OMS, showing the concentric lamellae. (D−F) showed that cell attachment efficiency remained high after the matrix-rolling procedure. (G−I) showed the morphology of one single OLC within an OMS, which was generated *via* cryosection, indicating that the cell integrity and matrix structure were not hampered by the matrix-rolling procedure. Green indicated FITC-labeled GelMA-based scaffold, red indicated actin-binding phalloidin, and blue indicated the nucleus.

to accelerate PEG degradation in a controlled manner, but it is beyond the scope of this work and will not be covered herein.

The concentric lamellae are the most distinguishable features of osteons. A mature osteon typically has 4−8 layers of lamellae. This unique feature endows osteon with an adaption to inhibit microcrack growth and prevent fracture occurrence within the cortical bone. Currently, only two artificial approaches have been proposed to recapitulate the lamellar structure, the 3D printing technique,[28] and the electrospinning-rolling technique.[29−31] The latter approach exhibited superior effect in forming the concentric architecture; however, the accommodation of isolated osteocytes within each lamella can hardly be obtained with these approaches. In this work, we adopted the rolling technique by wrapping the OLC-laden nanofibrous matrix around a syringe needle to simulate the lamellae. Owing to the suitable mechanical strength of the patterned matrix (184 ± 27 MPa, shown in previous work,[11] it was achievable to roll the matrix to generate a concentric OMS structure (Figure 5A−C). To observe its influence on embedded OLCs, the OMS complexes were prepared for cryosection. The cross-sectional images of OMS showed that BMSC adhesion efficiency stayed similarly high, showing that the mechanical rolling did not deteriorate the cells (Figure 5D−F). Moreover, from the magnified cross-sectional images, it was exhibited that cell integrities were not impaired by the rolling process either, and meanwhile, single OLCs projected multiple dendrites inside the microchannels that penetrated across the lamellae (Figure 5G−I).

https://doi.org/10.1021/acsomega.4c04146
ACS Omega 2024, 9, 41368−41377

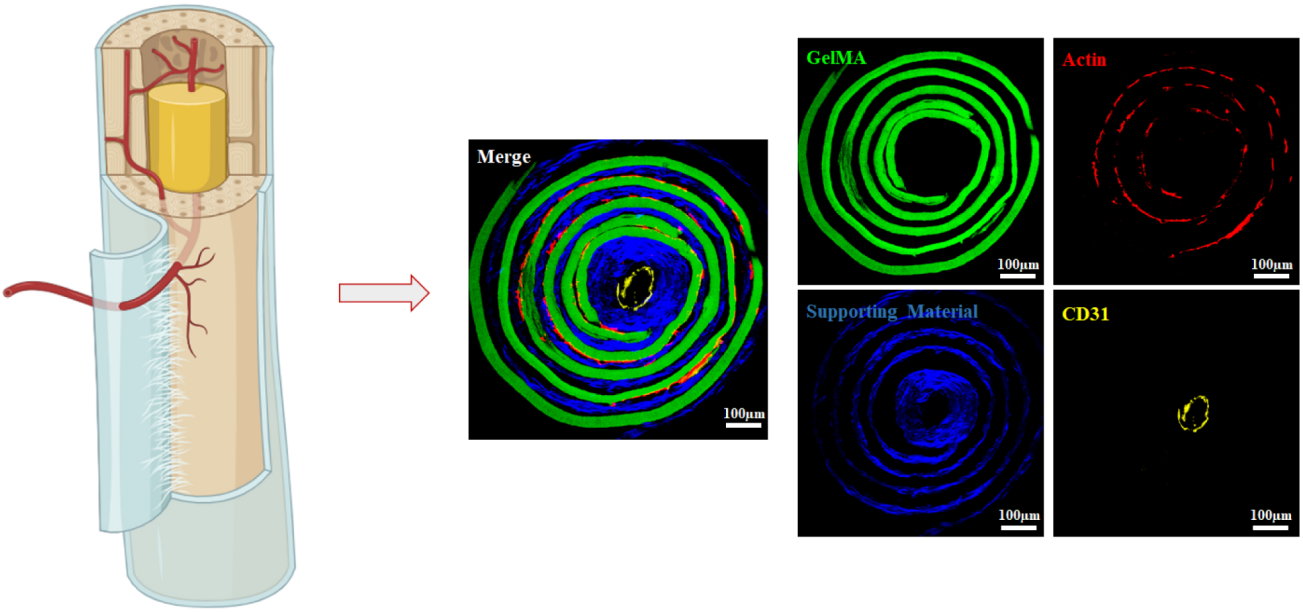

Figure 6. Recapitulation of the Haversian canal of the OMS system *via* injection of the HUVEC/Matrigel complex. Green indicated FITC-labeled GelMA-based scaffold, red indicated actin-binding phalloidin, yellow indicated CD31, a marker of endothelial cells, and blue indicated the cell nucleus and the dispersed Matrigel. The left picture was created with BioRender.com.

Haversian canals are the cylinder space surrounded by the innermost osteon lamella and are parallel to the main axis of an osteon. They not only encompass blood vessels and nerve fibers that provide nutrients and chemical signals to osteocytes but also transport osteoclastogenic and osteogenic cells to damaged sites to launch osteon remodeling. Therefore, the reconstruction of Haversian canals is of particular importance for osteon mimicking and cortical bone regeneration. Several techniques have been proposed to recapitulate this structure, including bottom-up,[32,33] casting,[34] extrusion,[35] and 3D printing;[36] however, an osteon-like spatial arrangement of the Haversian canal and the surrounding bone matrix was barely achieved. In this work, right after the patterned nanofibrous matrix was rolled around the syringe needle, an injection of the HUVEC/Matrigel complex into the central cylinder space formed by the rolling procedure was performed as the needle was retracted. As a result, the HUVEC/Matrigel complex formed a parallel axis inside the rolled matrix and after 3 days of culture, the HUVECs assembled into a ring-like structure, which emulated the morphology of a Haversian canal within an osteon (Figure 6).

It is to be noted that this OMS system was not applicable to *in vivo* bone regeneration yet. One major reason was that in this work, BMSCs were purposely separated from each other in order to simulate the *in vivo*–like osteocyte distribution. However, several previous studies have shown that the ALP-positive cell ratio of isolated MSCs (less than 10%) were significantly lower than that of clustered MSCs (over 75%),[37] which not only confirmed the critical role of intracellular communication in inducing osteogenic differentiation[37,38] but also indicated that single MSCs possessed attenuated potential in osteogenesis. Thus, the OMS system could barely induce bone regeneration. A second reason was related to the slow degradation of OMS. The orderly distribution of BMSCs were achieved by the PEG-initiated photolithography, but according to previous studies, PEGDA hydrogel remained stable for over 3 months *in vivo*.[39] Therefore, the scaffolds could hardly degrade before or at the time point required for bone matrix deposition and calcification, which further minimized the possibility of bone regeneration *via* OMS. Taken these limitations into consideration, this novel OMS system was more of an innovative model to explore the interaction among osteonal elements and inspire the development of next-generation tissue engineering strategies than a ready-to-use scaffold for cortical bone regeneration.

CONCLUSION

Osteons are the functional units of cortical bone; thus, a successful recapitulation of the integral osteon structure is the prerequisite for cortical bone regeneration. To date, the development of such bioinspired scaffolds to regenerate osteons and cortical bone is still in its infancy, which impedes the rapid functional recovery of bone. Here, we developed a novel hieratical scaffolding system based on a series of scaffolding and microfabrication techniques, including electrospinning, photolithography, laser-drilling, rolling, and 3D injection. By mimicking the bone ECM microenvironment that accommodates osteocytes, this novel system successfully induced the morphological and functional transition of BMSCs toward osteocytes and emulated the intracellular communication between osteocytes. Moreover, it recapitulated the osteonal structure comprehensively, thus setting a good example for the development of next-generation tissue engineering strategies for cortical bone regeneration. However, this system also has limitations. One is that its mechanical strength was relatively low compared to natural osteons, which was partially due to the lack of inorganic components. Moreover, it is not a ready-to-use scaffold for *in vivo* bone regeneration as aforementioned; instead, it comprised a study platform that allowed for detailed observation of the interaction between osteocytes and their accommodating microenvironment. Therefore, further in-depth exploration based on this work is still required for functional osteon regeneration.

https://doi.org/10.1021/acsomega.4c04146
ACS Omega 2024, 9, 41368−41377

AUTHOR INFORMATION

Corresponding Author

Bei Chang − *Hospital of Stomatology, Jilin Provincial Key Laboratory of Tooth Development and Bone Remodeling, Jilin University, Changchun 130021, China; Hospital of Stomatology, Department of Pediatric Dentistry, Jilin University, Changchun 130021, China;* orcid.org/0000-0001-5427-6545; Phone: 0431-85579567; Email: bchang@jlu.edu.cn

Authors

Xiheng Li − *Hospital of Stomatology, Jilin Provincial Key Laboratory of Tooth Development and Bone Remodeling, Jilin University, Changchun 130021, China; Hospital of Stomatology, Department of Pediatric Dentistry, Jilin University, Changchun 130021, China*

Yalu Sun − *Hospital of Stomatology, Jilin Provincial Key Laboratory of Tooth Development and Bone Remodeling, Jilin University, Changchun 130021, China; Hospital of Stomatology, Department of Pediatric Dentistry, Jilin University, Changchun 130021, China*

Shuangshuang Wang − *School and Hospital of Stomatology, Department of Oral Pathology, China Medical University, Shenyang 110001, China*

Chao Si − *Hospital of Stomatology, Jilin Provincial Key Laboratory of Tooth Development and Bone Remodeling, Jilin University, Changchun 130021, China; Hospital of Stomatology, Department of Pediatric Dentistry, Jilin University, Changchun 130021, China*

Huen Li − *Hospital of Stomatology, Jilin Provincial Key Laboratory of Tooth Development and Bone Remodeling, Jilin University, Changchun 130021, China; Hospital of Stomatology, Department of Pediatric Dentistry, Jilin University, Changchun 130021, China*

Complete contact information is available at: https://pubs.acs.org/10.1021/acsomega.4c04146

Author Contributions

Xiheng Li contributed to conceptualization, investigation, and writing—original draft preparation. Shuangshuang Wang contributed to methodology and data curation. Chao Si contributed to investigation, resources, and software. Huen Li contributed to visualization and formal analysis. Yalu Sun contributed to validation and visualization. Bei Chang contributed to supervision, project administration, writing—reviewing and editing, and funding acquisition

Notes

The authors declare no competing financial interest.

ACKNOWLEDGMENTS

This work was supported by Young Elite Scientists Sponsorship Program by CAST (YESS20210407), Natural Science Foundation of China (82101075), China Postdoctoral Science Foundation (2022M711301), Department of Science and Technology of Jilin Province (20240304039SF), Department of Finance of Jilin Provincial (JCSZ2021893-27), and Bethune Project of Jilin University (419161923025). The TOC figure was created with BioRender.com.

REFERENCES

(1) Campana, V.; Milano, G.; Pagano, E.; Barba, M.; Cicione, C.; Salonna, G.; Lattanzi, W.; Logroscino, G. Bone substitutes in orthopaedic surgery: from basic science to clinical practice. *J. Mater. Sci.: mater. Med* **2014**, *25* (10), 2445−2461.

(2) Greenwald, A. S.; Boden, S. D.; Goldberg, V. M.; Khan, Y.; Laurencin, C. T.; Rosier, R. N. Bone-graft substitutes: facts, fictions, and applications. *J. Bone Jt. Surg., Am. Vol* **2001**, *83* (2), S98−103.

(3) Zimmermann, G.; Moghaddam, A. Allograft bone matrix versus synthetic bone graft substitutes. *Injury* **2011**, *42*, S16−S21.

(4) Carter, C. B.; Norton, M. G. *Ceramic Materials: Science and Engineering*; Springer, 2007; Vol. *716*.

(5) Cancedda, R.; Giannoni, P.; Mastrogiacomo, M. A tissue engineering approach to bone repair in large animal models and in clinical practice. *Biomaterials* **2007**, *28* (29), 4240−4250.

(6) Weiner, S.; Traub, W.; Wagner, H. D. Lamellar bone: structure−function relations. *J. Struct. Biol* **1999**, *126* (3), 241−255.

(7) Petrtýl, M.; Heřt, J.; Fiala, P. Spatial organization of the haversian bone in man. *J. Biomech* **1996**, *29* (2), 161−169.

(8) Lin, Z. X.; Xu, Z.-H.; An, Y. H.; Li, X. In situ observation of fracture behavior of canine cortical bone under bending. *Mater. Sci. Eng* **2016**, *62*, 361−367.

(9) O'Brien, F. J.; Taylor, D.; Lee, T. C. Microcrack accumulation at different intervals during fatigue testing of compact bone. *J. Biomech* **2003**, *36* (7), 973−980.

(10) Chang, B.; Liu, X. Osteon: Structure, Turnover, and Regeneration. *Tissue Eng. Part B Rev* **2022**, *28* (2), 261−278.

(11) Ma, C.; Chang, B.; Jing, Y.; Kim, H.; Liu, X. Bio-Inspired Micropatterned Platforms Recapitulate 3D Physiological Morphologies of Bone and Dentinal Cells. *Adv. Sci* **2018**, *5*, 1801037.

(12) Chang, B.; Ma, C.; Feng, J.; Svoboda, K. K. H.; Liu, X. Dental Pulp Stem Cell Polarization: Effects of Biophysical Factors. *J. Dent. Res* **2021**, *100* (10), 1153−1160.

(13) Yu, B.; Pacureanu, A.; Olivier, C.; Cloetens, P.; Peyrin, F. Assessment of the human bone lacuno-canalicular network at the nanoscale and impact of spatial resolution. *Sci. Rep* **2020**, *10* (1), 4567.

(14) Bakker, A. D.; Klein-Nulend, J. Mechanisms of osteocyte mechanotransduction. *Clin. Rev. Bone Miner. Metab* **2010**, *8* (4), 163−169.

(15) Nguyen, A. M.; Jacobs, C. R. Emerging role of primary cilia as mechanosensors in osteocytes. *Bone* **2013**, *54* (2), 196−204.

(16) Geoghegan, I. P.; Hoey, D. A.; McNamara, L. M. Integrins in osteocyte biology and mechanotransduction. *Curr. Osteoporos. Rep* **2019**, *17* (4), 195−206.

(17) Thi, M. M.; Suadicani, S. O.; Schaffler, M. B.; Weinbaum, S.; Spray, D. C. Mechanosensory responses of osteocytes to physiological forces occur along processes and not cell body and require $\alpha V\beta 3$ integrin. *Proc. Natl. Acad. Sci. U.S.A* **2013**, *110* (52), 21012−21017.

(18) Wu, D.; Schaffler, M. B.; Weinbaum, S.; Spray, D. C. Matrix-dependent adhesion mediates network responses to physiological stimulation of the osteocyte cell process. *Proc. Natl. Acad. Sci. U.S.A* **2013**, *110* (29), 12096−12101.

(19) Cardoso, L.; Herman, B. C.; Verborgt, O.; Laudier, D.; Majeska, R. J.; Schaffler, M. B. Osteocyte apoptosis controls activation of intracortical resorption in response to bone fatigue. *J. Bone Miner. Res* **2009**, *24* (4), 597−605.

(20) Kennedy, O. D.; Laudier, D. M.; Majeska, R. J.; Sun, H. B.; Schaffler, M. B. Osteocyte apoptosis is required for production of osteoclastogenic signals following bone fatigue in vivo. *Bone* **2014**, *64*, 132−137.

(21) Bromage, T. G.; Lacruz, R. S.; Hogg, R.; Goldman, H. M.; McFarlin, S. C.; Warshaw, J.; Dirks, W.; Perez-Ochoa, A.; Smolyar, I.; Enlow, D. H.; Boyde, A. Lamellar bone is an incremental tissue reconciling enamel rhythms, body size, and organismal life history. *Calcif. Tissue Int* **2009**, *84* (5), 388−404.

(22) Milovanovic, P.; Zimmermann, E. A.; Hahn, M.; Djonic, D.; Püschel, K.; Djuric, M.; Amling, M.; Busse, B. R. Osteocytic canalicular networks: morphological implications for altered mechanosensitivity. *ACS Nano* **2013**, *7* (9), 7542−7551.

(23) Capulli, M.; Paone, R.; Rucci, N. Osteoblast and osteocyte: games without frontiers. *Arch. Biochem. Biophys* **2014**, *561*, 3−12.

(24) Bonewald, L. F. The amazing osteocyte. *J. Bone Miner. Res* **2011**, *26* (2), 229−238.
(25) Zhang, K.; Barragan-Adjemian, C.; Ye, L.; Kotha, S.; Dallas, M.; Lu, Y.; Zhao, S.; Harris, M.; Harris, S. E.; Feng, J. Q.; Bonewald, L. F. E11/gp38 selective expression in osteocytes: regulation by mechanical strain and role in dendrite elongation. *Mol. Cell. Biol* **2006**, *26* (12), 4539−4552.
(26) Palumbo, C.; Palazzini, S.; Marotti, G. Morphological study of intercellular junctions during osteocyte differentiation. *Bone* **1990**, *11* (6), 401−406.
(27) Whitson, S. W. Tight junction formation in the osteon. *Clin. Orthop. Relat. Res* **1972**, *86*, 206−213.
(28) Piard, C.; Baker, H.; Kamalitdinov, T.; Fisher, J. Bioprinted osteon-like scaffolds enhance in vivo neovascularization. *Biofabrication* **2019**, *11* (2), 025013.
(29) Andric, T.; Sampson, A.; Freeman, J. Fabrication and characterization of electrospun osteon mimicking scaffolds for bone tissue engineering. *Mater. Sci. Eng* **2011**, *31* (1), 2−8.
(30) Hejazi, F.; Mirzadeh, H. Roll-designed 3D nanofibrous scaffold suitable for the regeneration of load bearing bone defects. *Prog. Biomater* **2016**, *5* (3−4), 199−211.
(31) Barati, D.; Karaman, O.; Moeinzadeh, S.; Kader, S.; Jabbari, E. Material and regenerative properties of an osteon-mimetic cortical bone-like scaffold. *Regener. Biomater* **2019**, *6* (2), 89−98.
(32) Zuo, Y.; Xiao, W.; Chen, X.; Tang, Y.; Luo, H.; Fan, H. Bottom-up approach to build osteon-like structure by cell-laden photocrosslinkable hydrogel. *Chem. Commun* **2012**, *48* (26), 3170−3172.
(33) Zuo, Y.; Liu, X.; Wei, D.; Sun, J.; Xiao, W.; Zhao, H.; Guo, L.; Wei, Q.; Fan, H.; Zhang, X. Photo-cross-linkable methacrylated gelatin and hydroxyapatite hybrid hydrogel for modularly engineering biomimetic osteon. *ACS Appl. Mater. Interfaces* **2015**, *7* (19), 10386−10394.
(34) Despang, F.; Bernhardt, A.; Lode, A.; Dittrich, R.; Hanke, T.; Shenoy, S.; Mani, S.; John, A.; Gelinsky, M. Synthesis and physicochemical, in vitro and in vivo evaluation of an anisotropic, nanocrystalline hydroxyapatite bisque scaffold with parallel-aligned pores mimicking the microstructure of cortical bone. *J. Tissue Eng. Regener. Med* **2015**, *9* (12), No. E152−E166.
(35) Wei, D.; Sun, J.; Bolderson, J.; Zhong, M.; Dalby, M. J.; Cusack, M.; Yin, H.; Fan, H.; Zhang, X. Continuous fabrication and assembly of spatial cell-laden fibers for a tissue-like construct via a photolithographic-based microfluidic chip. *ACS Appl. Mater. Interfaces* **2017**, *9* (17), 14606−14617.
(36) Zhang, M.; Lin, R.; Wang, X.; Xue, J.; Deng, C.; Feng, C.; Zhuang, H.; Ma, J.; Qin, C.; Wan, L.; Chang, J. 3D printing of Haversian bone−mimicking scaffolds for multicellular delivery in bone regeneration. *Sci. Adv* **2020**, *6* (12), No. eaaz6725.
(37) McBeath, R.; Pirone, D. M.; Nelson, C. M.; Bhadriraju, K.; Chen, C. S. Cell shape, cytoskeletal tension, and RhoA regulate stem cell lineage commitment. *Dev. Cell* **2004**, *6* (4), 483−495.
(38) Tang, J.; Peng, R.; Ding, J. The regulation of stem cell differentiation by cell-cell contact on micropatterned material surfaces. *Biomaterials* **2010**, *31* (9), 2470−2476.
(39) Browning, M. B.; Cereceres, S. N.; Luong, P. T.; Cosgriff-Hernandez, E. M. Determination of the in vivo degradation mechanism of PEGDA hydrogels. *J. Biomed Mater. Res. A* **2014**, *102* (12), 4244−4251.

https://doi.org/10.1021/acsomega.4c04146
ACS Omega 2024, 9, 41368−41377